

Radiation coupling and image formation in scanning near-field optical microscopy

D.W. Pohl^{a,*}, L. Novotny^b, B. Hecht^a, H. Heinzelmann^c

^a IBM Research Division, Zurich Research Laboratory, Säumerstr. 4, CH-8803 Rüschlikon, Switzerland

^b Institut für Feldtheorie und Höchstfrequenztechnik, Swiss Federal Institute of Technology (ETH), CH-8092 Zürich, Switzerland

^c Institut für Physik, University of Basel, Klingelbergstr. 82, CH-4056 Basel, Switzerland

Abstract

The propagation of light through an aperture scanning near-field optical microscope is studied. Rules for optimizing the confinement and throughput of aperture near-field probes are derived. The radiation from the aperture through simple sample structures, a flat substrate and a substrate with stripe-like elevations and depression, into classically allowed and forbidden directions is determined quantitatively. It is shown that small amplitude and phase objects can be distinguished by comparing “allowed” and “forbidden” light images.

Keywords: Nanostructures; Optical properties

1. Introduction

The wealth of optical phenomena offers attractive opportunities for interaction with the world of mesoscopic dimensions: (i) if the relevant radiation fields can be made sufficiently intense in a sufficiently confined interaction volume, and (ii) if the radiation emerging from such a confined volume can be detected with sufficient sensitivity and selectivity. Confinement into volumes less than 100 nm in diameter, i.e. considerably smaller than the wavelength, is possible only by means of material structures that have such small dimensions themselves. Small apertures, small particles acting as scattering centers, and pointed metallic or dielectric tips are suitable for this purpose (Fig. 1). When integrated into a scanning probe microscope, such structures can provide optical scan images with resolution in the sub-100 nm regime.

The most popular microscope operating on this principle is the aperture scanning near-field optical microscope (SNOM, also called NSOM) [1–13], which is based on a design we developed ten years ago [1–3]. In the present paper we report on recent, mainly computational studies [14–16] of: (i) the light flux from the far field to a subwavelength-diameter aperture in a metallic screen, (ii) the interaction with amplitude and phase objects, and (iii) the subsequent spreading of the transmitted radiation. The multiple multipole (MMP) method [17,18] was used to calculate the electro-

magnetic fields in all the SNOM configurations considered so far because of its efficiency and precision. Knowledge of these properties is instrumental to the design of efficient near-field optical microscopes. Complementary experiments are described in the paper of Heinzelmann et al. [19] from these proceedings and in Refs. [12] and [13].

2. Illuminating a subwavelength-diameter aperture

A scanning aperture optical probe logically consists of a conical or pyramidal transparent body with a frustrated apex coated with metal such that the sidewalls are opaque but a transparent hole is left at the apex (Fig. 2(a) and 2(b)). The transparent body may be the corner of a faceted quartz crystal [1–3], a micropipette [4], an optical fiber that has been pulled [8] or etched [20,21] to form a sharp tip at one end, or a transparent micromechanic cantilever with tip [19,22,23]. The coating is usually obtained by evaporating an Al film of 100–200 nm thickness. As the aperture diameters of interest are much smaller than the wavelength (even inside the probe), all waveguide modes run into cutoff before reaching the apex. An extremely small fraction of the input power only “tunnels” to and through the aperture; see, for example, Refs. [3,15].

Optimization of the optical probe shape for maximum light throughput and minimum spot size is instrumental for the advancement of the SNOM technique, be it with regard to

* Corresponding author.

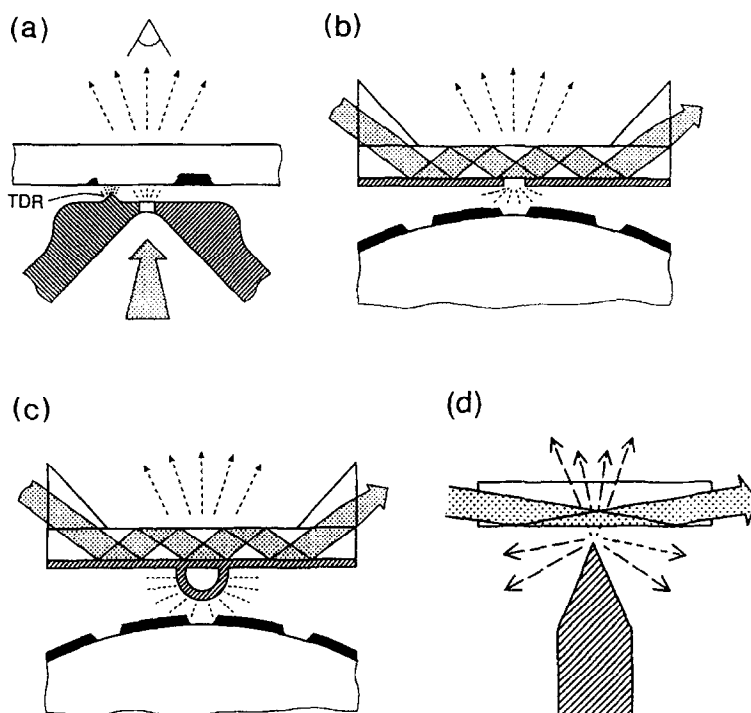


Fig. 1. Structures suitable for nanometer confinement of optical radiation: aperture in a metallic screen at (a) the apex of a transparent tip and (b) a flat waveguide structure; scattering center, illuminated through (c) a flat waveguide or (d) by an evanescent wave excited at the object surface. (a), (b), (c) from Ref. [7].

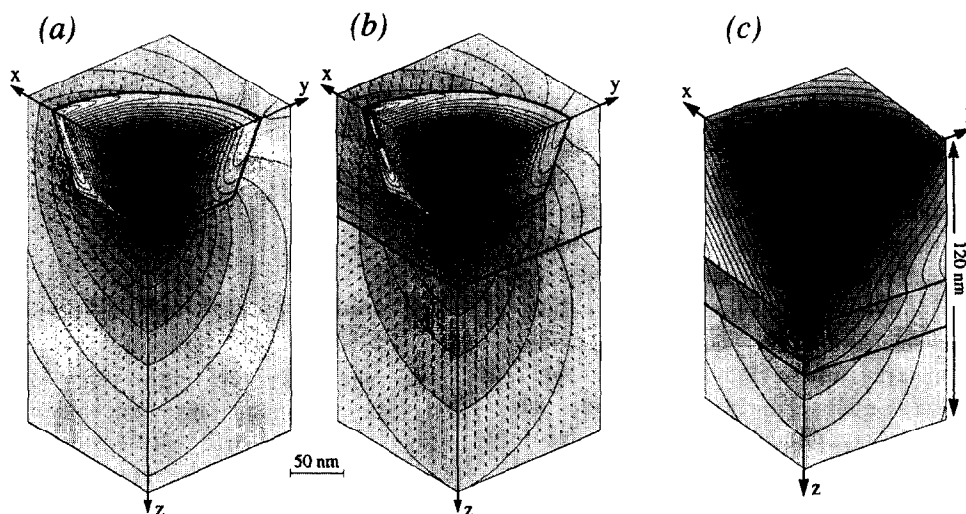


Fig. 2. Aluminum-coated aperture SNOM tips with contour plots of the electrical energy density (constant $|\mathbf{E}|^2$, factor of two between successive lines, polarization in the plane $y=0$). (a), (b) open aperture, diameter = 50 nm, wall thickness = 70 nm, arrows: direction of Poynting vector. (c) Entirely coated (CTC) probe, wall thickness infinite, $\alpha = 30^\circ$, $R = 10$ nm, $D = 5$ nm, $z_G = 20$ nm. In (b), (c), a glass substrate with $\epsilon_s = 2.25$ has been approached to the aperture. (a), (b) from Ref. [15], (c) from Ref. [16].

resolution, detection of faint signals such as in near-field infrared microscopy [24], or photochemical/photophysical modification on the nanometer scale. We therefore studied the influence of the cone angle on throughput and spot size [16].

The common open, transparent (hollow) frustum-shaped (OTF) aperture (Fig. 3(a) and 3(b)) produces a double-

peaked intensity distribution in the exit plane [25] (cf. Fig. 3(a) and 4(a) (dotted curve)). The quasi-singularities in the plane of polarization are caused by the extreme curvature of the rim of the aperture ("lightning rod effect"). We therefore also studied an alternative "aperture" optical probe, which does not have a sharp rim, but has the shape of a frustum topped by a spherical transparent calotte, metal

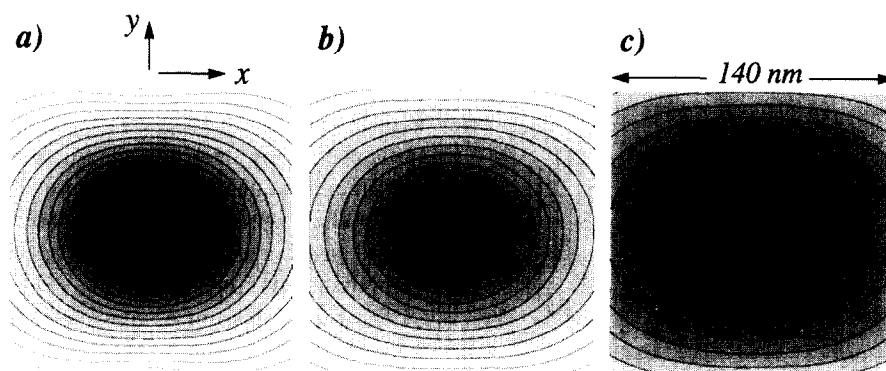


Fig. 3. Intensity ($|E|^2$, factor of $2^{1/2}$ between contour lines) evaluated in a plane 1 nm in front of (a) of an OTF, 50 nm diameter, $\alpha = 10^\circ$; (b), (c) of CTC probes with $R = 10$ nm, $D = 3$ nm, $\alpha = 30^\circ$ and 75° . From Ref. [16].

coated such that the film thickness at the apex is less than the optical skin depth in the apex region [16] (Fig. 3c) and hence is semitransparent.

In the models used for computational determination of the optical fields, the OTF or the coated transparent calotte (CTC) probe is connected to a cylindrical waveguide at the wide end. For the latter, assumed to extend to infinity in the z direction, exact analytical solutions in the form of waveguide modes are known [26]. The cylinder diameter is 200 nm, which guarantees that the HE_{11} mode we chose for excitation is in the propagating regime for the wavelength used in our calculations, $\lambda = 488$ nm. The incident radiation is polarized in the x direction. The chosen dielectric constants $\epsilon_c = 2.16$, $\epsilon_m = -34.5 + 8.5i$ of the transparent core and the metallic coating refer to quartz glass and aluminum. The probe tip is either in free space or mounted above a flat glass substrate with $\epsilon_s = 2.25$ at a distance z_G .

The shape of the OTF probe is characterized by the taper angle ($\alpha \equiv 1/2$ cone angle) and the diameter of the core in the exit plane, 10° and 50 nm, respectively, in the examples to be shown here. The CTC probe shape is determined by the taper angle of the conical part, the radius R of the calotte, and the thickness D of the coating at the apex. All three parameters were varied in the course of our investigations to better understand their influence on the resulting field distributions.

Some field distributions are shown in Fig. 2 in the form of contour plots of the square modulus of the electric field $|E|^2$. Only the foremost parts of OTF and CTC SNOM probes are depicted. The arrows indicate the flux of radiation (time-averaged Poynting vector). In the (y, z) plane the electric field is parallel to the glass/metal and metal/air interfaces and of almost vanishing intensity. In the (x, z) plane the electric field everywhere has a component perpendicular to the interface, and the contour lines are hence discontinuous. The fast decay towards the end of the probe [15] is a result of overdamping. To the sides, the fields decay exponentially into the aluminum cladding, where a considerable amount of the incident power is dissipated.

Contour plots of the field distributions 1 nm in front of the exit plane are shown in Fig. 3. The double peak structure (Fig. 3(a)) is produced by the 50 nm diameter OTF probe,

whereas Fig. 3(b) and 3(c) stem from CTC probes having taper angles of 30° and 75° , respectively. Their near fields have only one sharp maximum, which allows more unambiguous imaging conditions and a smaller overall spot size. This is displayed more clearly in the intensity cross-sections in Fig. 4(a). With increasing distance z_G from the exit plane (Fig. 4(b)), the fields decay rapidly, having a gradient com-

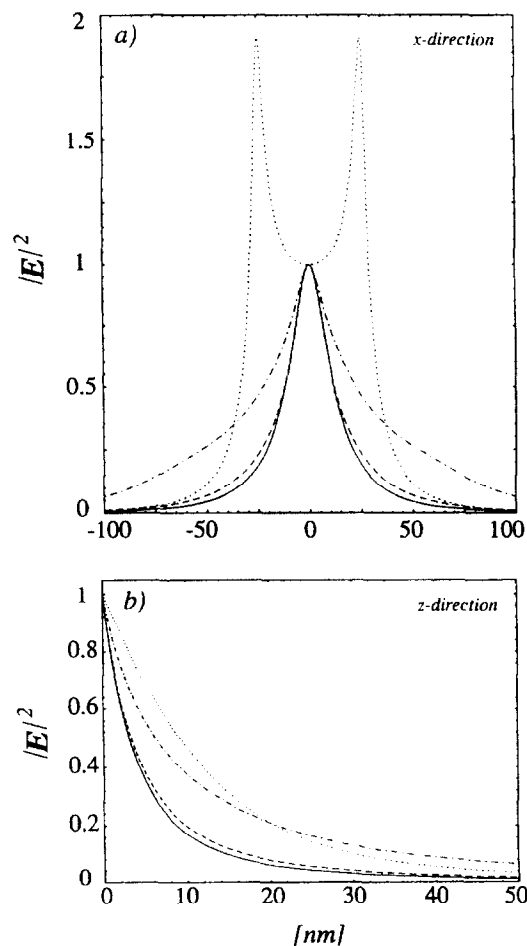


Fig. 4. Intensity ($|E|^2$) along the (a) x . (b) z direction of Fig. 2. Dotted line, 50 nm open aperture; solid line, CTC, $\alpha = 15^\circ$, $D = 3$ nm, $R = 10$ nm; dashed line, same except $\alpha = 45^\circ$; dash-dotted line, same except $\alpha = 80^\circ$. From Ref. [16].

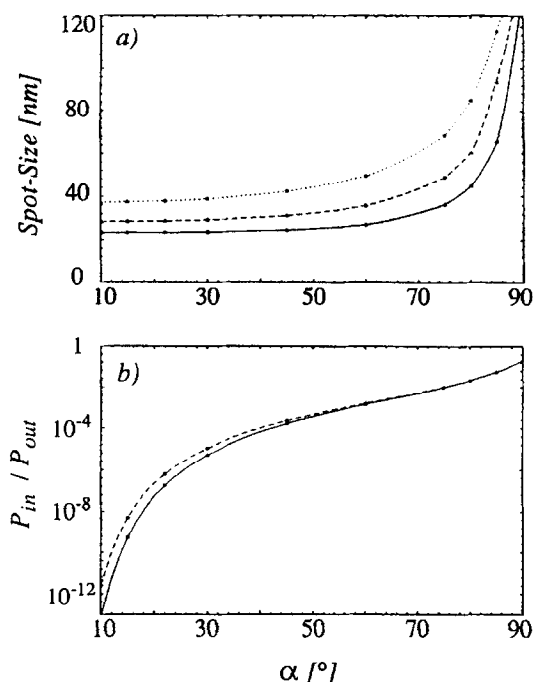


Fig. 5. (a) Spot size and (b) transmission of CTC probes as a function of taper angle. (a) $R = 10$ nm; $D = 3$ nm (solid line), 5 nm (dashed line), 10 nm (dotted line). (b) $D = 3$ nm; $R = 5$ nm (solid line) and 10 nm (dashed line). From Ref. [16].

parable with that in lateral directions. It is seen that the CTC spot size in all three dimensions is of the order of 20 nm for taper angles of both 15° and 45° . The interaction volume can hence be kept extremely small with CTC optical probe tips.

The spot size, defined as the average between the FWHM of $|\mathbf{E}|^2$ along the x and y directions, and the total transmitted light flux are plotted in Fig. 5 as a function of the cone angle. The spot size (Fig. 5(a)) evaluated for three values of D and $R = 10$ nm, $z_G = 1$ nm remains almost constant up to about $\alpha > 60^\circ$. The power transmission (Fig. 5(b)), however, grows enormously with increasing taper angle.

Whereas the data obtained refer to operation at $\lambda = 488$ μm , a glass core, and an Al coating, similar behavior may be expected for other wavelengths and other materials. The present results therefore allow us to define in principle the shape of the optimum (CTC) aperture SNOM probe:

- (half) angle of apex, $\alpha = 30^\circ$ to 60° ;
- radius of curvature, $R \rightarrow 0$;
- residual coating thickness, $D \rightarrow 0$.

Such large-angle probes will be particularly useful for fluorescence and modification experiments, which depend in a critical way on a sufficiently high light flux.

CTC probes can be produced in a similar way to OTF probes. A sufficiently thin coating of the apex can be achieved by appropriately adjusting the evaporation source used for sidewall coating or by deposition of an additional thin metal film onto the apex. As pulling of fibers usually leads to taper angles smaller than 20° , etching techniques [1,20,21] may be superior. Etched crystals, in particular, may have atomically sharp apices that approach the ideal of vanishing R .

3. Radiation from a small aperture

As complicated as the influx of radiation to the aperture zone is so is its outflux, even if we ignore for the moment the influence of any interrogated structured object. What is the “diffraction pattern” of an aperture of subwavelength diameter? What happens if it is approached to a flat substrate? Sound answers to these questions again require considerable computational effort.

The radiation from a subwavelength-size aperture turns out to be emitted most strongly not in the forward direction but at an angle in the direction of polarization (cf. Fig. 2). Upon approaching a substrate with $\epsilon_s = 2.25$, the total transmitted light flux increases significantly (compare equivalent contour lines in Fig. 2(a) and 2(b)). Some of the flux is scattered around the probe and couples to modes of the external surface, propagating with strong radiative losses into the backward direction.

Most of the extra light, however, is radiated into the substrate at angles larger than the critical one given by $\theta_{cr} = \arcsin(\epsilon_s^{-1/2})$. The rapidly decaying field in the proximity of the aperture can excite total internal reflection (TIR)-type evanescent waves at the dielectric interface. Such waves represent radiative interface modes. The direction of emission is determined by the requirement that the component of the k vectors parallel to the surface be conserved (“inverse” TIR). This finding led to the development of the forbidden-light or tunnel SNOM (TNOM) [12,13,19].

The integrated light flux Φ vs. gap width z_G is shown in Fig. 6 for various observation conditions [15]; namely θ , 70° ; angle of acceptance, 10° ; x, z plane (solid curve); total radiation into the forbidden regime (dash-dotted curve), into the allowed one (dotted curve), and into the entire hemisphere under the probe tip. In the first case, the decay length exactly equals that of a TIR evanescent wave excited by a plane wave incident at $\theta = 70^\circ$, as to be expected on the basis of the reciprocity principle. The much larger signal from the

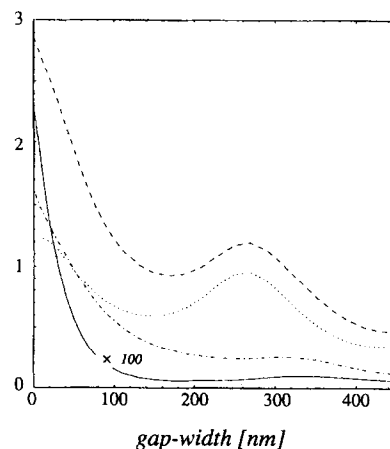


Fig. 6. Light flux into far field vs. gap width (OTF) of Fig. 2 but with infinite cladding. Dashed curve, total flux; dash-dotted curve, forbidden zone; dotted curve, allowed zone; solid curve, $y = 0$ plane, $\theta = 70^\circ$, angle of acceptance = 10° . From Ref. [15].

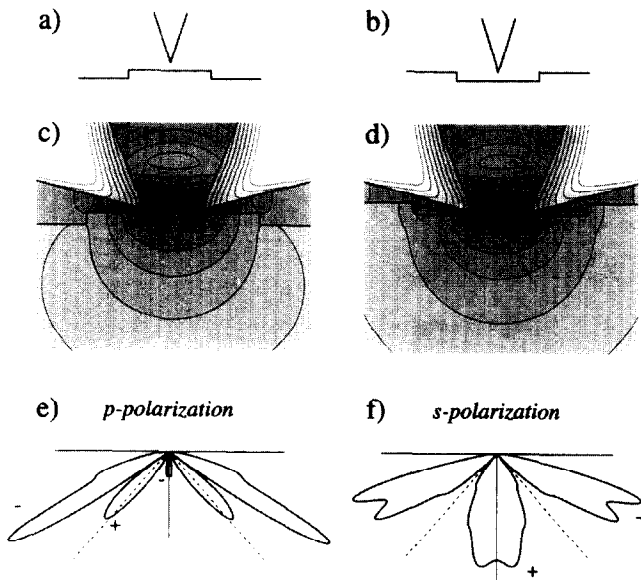


Fig. 7. SNOM probe scanning a glass grating: Are (a) “top” and (b) “valley” positions optically equivalent? (c), (d) Computed electrical energy distributions, 2D model, p polarization. From Ref. [13]. (e), (f) Radiation patterns, difference between top and bottom positions.

total forbidden radiation also shows an almost exponential, though less abrupt, distance dependence, whereas the flux coupled into the allowed zone is dominated by interference undulations that provide little unambiguous information about the gap width.

It should be noted that forbidden light, being excited efficiently only for gap widths $< 1 \mu\text{m}$, is quite insensitive to stray light emerging, for instance, from pinholes at the shank of the optical probe. It is therefore possible to obtain high-contrast images in the TNOM mode, even with optical probes that are unsuitable for standard SNOM [13].

We next turn to two very simple object structures: a narrow, low height (8 nm), stripe-like elevation and a corresponding depression on an otherwise flat dielectric (glass) substrate (Fig. 7(a) and 7(b)) [13]. The elevation (depression) is assumed to be distinctly wider (190 nm) than the aperture diameter (50 nm), but still small compared with the wavelength (488 nm). If the SNOM signal depended only on the properties of the immediate proximity of the aperture, no

difference between the “top” and “bottom” positions indicated in the figure should exist; only the steps ought to appear in a SNOM image. Much experimental evidence [12,13,27,28], however, indicates that stripes 100–200 nm in width do indeed appear in SNOM images, bearing an obvious similarity to the topographic structure (Fig. 8) [13].

To understand this result, one might think of a number of mechanisms.

1. The glass in the surface layer of a valley might differ from the material of the elevation due to the manufacturing process.
2. The gap width is larger when the tip is above a valley because it cannot penetrate it completely.
3. Elevations and valleys may be considered to a first approximation as being convex and concave parts of the surface, respectively. These opposite curvatures may influence the spreading and propagation of the transmitted radiation.

Careful inspection of the topography recorded by means of the shear force detector built into the SNOM [12,13,19] as well as by a standard AFM, however, gave no evidence of increased roughness in the valleys. We therefore believe that differences in surface structure are insignificant, in agreement with the manufacturer [29]. Comparison with the experimentally observed contrast further rules out the second hypothesis because the valleys are brighter than the elevations in forbidden light, opposite to what one would expect on the basis of the approach curves in Fig. 6. The observed behavior, however, is in agreement with hypothesis 3 in so far as the laws of classical optics would predict a focusing effect for the convex elevation, i.e. a concentration of radiation in the forward direction, and the opposite for the concave valley.

To substantiate this assumption, the influence of surface curvature was studied numerically, simulating the electromagnetic fields in the geometries sketched in Fig. 7(a) and 7(b). Computations were restricted to the two-dimensional model SNOM introduced previously [14] because the resulting field distributions strongly resemble those of the corresponding three-dimensional configuration [15].

Fig. 7(c) and 7(d) depict the computed near fields for p (TM) polarization (with regard to stripe orientation) for “top” and “valley” positions of the optical probe. One

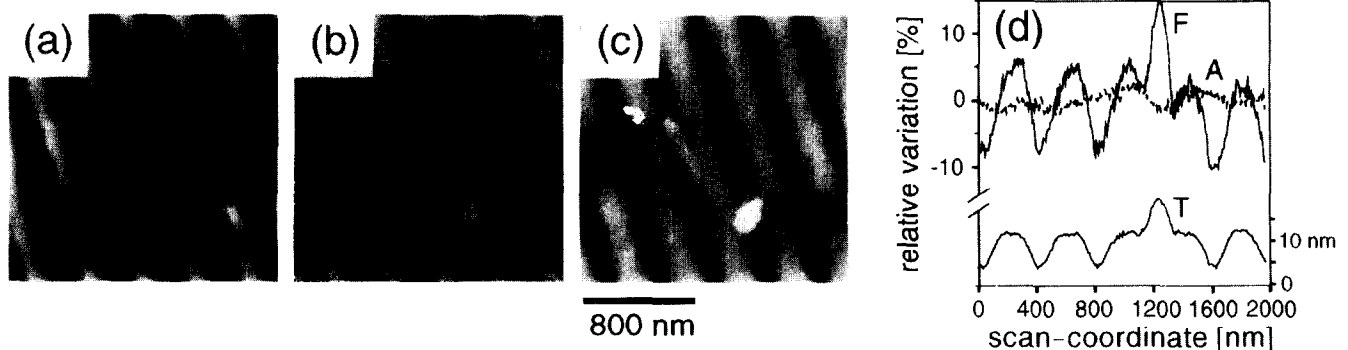


Fig. 8. Images of a bare glass grating with period 383 nm, step height 8 nm (prepared by B. Curtis, PSI Zurich), polarization perpendicular to grating lines. (a) forbidden light; (b) allowed light; (c) topography (friction image); (d) scan lines. A, allowed, F, forbidden light; T, topography. From Ref. [13].

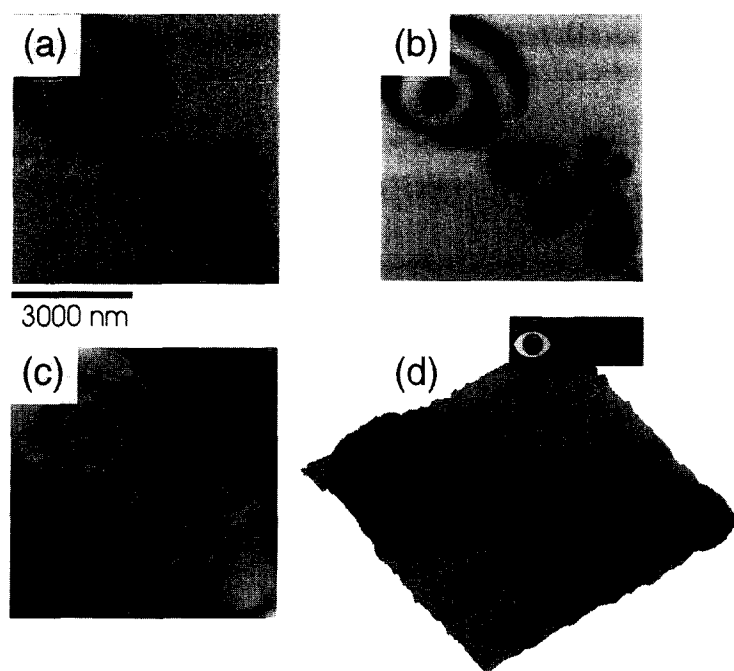


Fig. 9. Lithographic "eye-bee(M)" logo, 5 nm Ti + 5 nm Au, seen with (a) forbidden, (b) allowed light, (c) with the "shear force" detector, (d) superposition of (a) and (c).

clearly sees the focusing/defocusing effects of the two topographies. A similar but smaller variation exists for the near fields of *s*- (TE)-polarized light. The differences between the radiation patterns of top and bottom positions are plotted in Fig. 7(e) and 7(f) for *p* and *s* polarization. For both polarizations, the side lobes, which represent the forbidden radiation, are negative, meaning that elevations indeed appear darker than depressions. The opposite is true for the forward lobes, which represent the allowed light. The calculated contrast is compared in Table 1 with experimental values from Fig. 8. The direction of observation was in the plane of polarization, almost perpendicular to the direction of the stripes, corresponding to *p* polarization. The contrast is defined as $2(\Phi_{\text{top}} - \Phi_{\text{valley}})/(\Phi_{\text{top}} + \Phi_{\text{valley}})$. The agreement both with regard to the sign and to the improved contrast of the forbidden image is remarkable. (The close proximity of the numerical values is considered coincidental.)

One has to conclude that the recorded light flux does not depend on the local optical properties of the object alone but also on the environment within a distance of several aperture diameters. A number of previous theoretical investigations actually arrived at similar results, see, for example, Refs. [30] and [31]; these studies, however, did not allow direct comparison with our experimental results because the models used differed significantly from the present TNOM set-up.

Table 1

Contrast of elevations and depressions of a glass grating; comparison between 2D model SNOM and experiment [13]

Contrast (%)	Calc. <i>s</i> pol.	Calc. <i>p</i> pol.	Exp. <i>p</i> pol.
Allowed	1.6	3.4	4
Forbidden	-5.6	-10.1	-12

Non-local effects are also known to have an influence on images obtained by scanning tunneling microscopy and AFM. The "interference patterns" recorded in Eigler et al.'s famous quantum corral experiment [32], for instance, fall into this category, as do the difficulties in imaging soft tissues with AFM. In both cases it is still possible to recognize very small structures, the signatures of which are superimposed on longer range structures. This is obviously also the case in the present near-field optical investigation.

Very small objects such as the imperfections (dust particles?) seen on top of the grating in Fig. 8, which we believe to be phase objects, have been found to appear with reverse contrast in allowed and forbidden light images, again in agreement with numerical simulations. The signature of amplitude objects, however, is negative contrast in both types of images, cf. for instance Fig. 9, which shows an artistic version of IBM's logo (*I* = eye, *B* = bee) implemented by lithographic techniques as a 5 nm titanium plus 5 nm gold semitransparent layer on glass. Forbidden light images combined with allowed light images hence allow one to distinguish between the amplitude and the phase object, which is instrumental for quantitative image interpretation.

4. Summary

The results of our investigations suggest the following.

- The optimum aperture optical probe is a wide-angle, sharply pointed transparent tip entirely coated but transparent at the apex.
- A sizable portion of the light transmitted by the optical probe into the object flows in the forbidden directions.

- SNOM images represent a superposition of strictly local and non-local contributions from the near-field range.
- Images obtained with forbidden light provide high contrast and are insensitive to stray light.
- Small phase objects can be distinguished from amplitude objects by comparing forbidden and allowed images.

Acknowledgements

We thank Ch. Hafner and O.J.F. Martin for many illuminating discussions, and B. Curtis and H. Rothuizen, who kindly provided us with glass grating and the “eye-bee-M” logo, respectively. This work is supported in part by the Swiss National Science Foundation and by a grant from the priority program OPTIQUE of the Board of the Swiss Federal Institutes of Technology.

References

- [1] D.W. Pohl, W. Denk and M. Lanz, Optical stethoscopy: image recording with resolution $\lambda/20$, *Appl. Phys. Lett.*, **44** (1984) 651.
- [2] D.W. Pohl, W. Denk and U. Dürig, Optical stethoscopy: imaging with $\lambda/20$, *SPIE*, **565** (1985) 56.
- [3] U. Dürig, D.W. Pohl and F. Rohner, Near-field optical scanning microscopy, *J. Appl. Phys.*, **59** (1986) 3318.
- [4] E. Betzig, M. Isaacson and A. Lewis, Collection mode near-field scanning optical microscopy, *Appl. Phys. Lett.*, **51** (1987) 2088.
- [5] E. Betzig, J.K. Trautman, T.D. Harris, J.S. Weiner and R.L. Kostelak, Breaking the diffraction barrier: optical microscopy on a nanometric scale, *Science*, **251** (1991) 1468.
- [6] D.W. Pohl, U.Ch. Fischer and U.T. Dürig, Scanning near-field optical microscopy (SNOM): basic principles and some recent developments, *SPIE*, **897** (1988) 84.
- [7] D.W. Pohl, Scanning near-field optical microscopy (SNOM), *Advances in Optical and Electron Microscopy*, Vol. 12, Academic Press, London, 1991, pp. 243–312.
- [8] E. Betzig and J. Trautman, Near-field optics: microscopy, spectroscopy and surface modification beyond the diffraction limit. *Science*, **257** (1992) 189.
- [9] M. Vaez-Iravani and R. Toledo-Crow, Pure linear polarization imaging in near-field scanning optical microscopy, *Appl. Phys. Lett.*, **63** (1993) 138.
- [10] M. Fujihira, H. Monobe, H. Muramatsu and T. Ataka, Scanning near-field fluorescence microscopy and nanoscopic fluorescence spectroscopy in combination with a noncontact scanning force microscope, *Chem. Lett.*, **3** (1994) 657.
- [11] H. Heinzelmann and D.W. Pohl, Scanning near-field optical microscopy, *Appl. Phys. A*, **59** (1994) 89.
- [12] B. Hecht, H. Heinzelmann and D.W. Pohl, Combined aperture SNOM/PSTM: Best of both worlds? *Ultramicroscopy*, **57** (1994) 228.
- [13] B. Hecht, D.W. Pohl, H. Heinzelmann and L. Novotny, Tunnel near-field optical microscopy: TNOM-2, in O. Marti and R. Möller (eds.), *Photons and Local Probes*, NATO ASI Series E: Appl. Sci., Kluwer, Dordrecht, **300** (1995) 93.
- [14] L. Novotny, D.W. Pohl and P. Regli, Light propagation through nanometer-sized structures: the two-dimensional aperture scanning near-field optical microscope, *J. Opt. Soc. Am. A*, **11** (1994) 1768.
- [15] L. Novotny and D.W. Pohl, Light propagation in scanning near-field optical microscopy, in O. Marti and R. Möller (eds.), *Photons and Local Probes*, NATO ASI Series E: Appl. Sci., Kluwer, Dordrecht, p. 21.
- [16] L. Novotny, D.W. Pohl and B. Hecht, Scanning near-field optical probe with ultra-small spot size, *Optics Lett.*, **20** (1995) 970.
- [17] Ch. Hafner, *The Generalized Multiple Multipole Technique for Computational Electromagnetics*, Artech, Boston, MA, 1990.
- [18] Ch. Hafner and L.H. Bomholdt, *The 3d Electrodynamic Wave Simulator*, Wiley, Chichester, UK, 1993.
- [19] H. Heinzelmann, Th. Lacoste, Th. Huser, M. Rüetschi, W. Gutmannsbauer, H.-J. Güntherodt, B. Hecht and D.W. Pohl, Instrumental developments and recent experiments in near-field optical microscopy, *Thin Solid Films*, **273** (1996) 149.
- [20] T. Pangaribuan, S. Jiang and M. Ohtsu, Highly controllable fabrication of fiber probe for photon scanning tunneling microscope, *Scanning*, **16** (1993) 362.
- [21] P. Tomanek, Fiber tips for reflection scanning near-field optical microscopy, in D.W. Pohl and D. Courjon (eds.), *Near Field Optics*, NATO ASI Series E: Appl. Sci., Vol. 242, Kluwer, Dordrecht, 1993, p. 295.
- [22] N.F. van Hulst, M.H.P. Moers, O.F.J. Noordman, R.G. Tack and F.B. Segerink, Near-field optical microscopy using a siliconnitride probe, *Appl. Phys. Lett.*, **62** (1993) 461.
- [23] F. Baida, D. Courjon and G. Tribillon, Combination of a fiber and a silicon nitride top as a bifunctional detector: first results and perspectives, in D.W. Pohl and D. Courjon (eds.), *Near Field Optics*, NATO ASI Series E: Appl. Sci., Vol. 242, Kluwer, Dordrecht, 1993, p. 71.
- [24] T. Nakano and S. Kawata, Evanescent field scanning microscope with Fourier transform infrared spectrometer, *Scanning*, **16** (1994) 368.
- [25] C.J. Bouwkamp, On Bethe’s theory of diffraction by small holes, *Philips Res. Rep.*, **66** (1950) 163.
- [26] L. Novotny and C. Hafner, Light propagation in a cylindrical waveguide with a complex, metallic dielectric function, *Phys. Rev. E*, **50** (1994) 4094.
- [27] C. Bainier, S. Leblanc and D. Courjon, Scanning tunneling optical microscopy: Application to very low relief objects, in D.W. Pohl and D. Courjon (eds.), *Near Field Optics*, NATO ASI Series E: Appl. Sci., Vol. 242, Kluwer, Dordrecht, 1993, p. 97.
- [28] F. de Fornel, E. Bourillot, P. Adam, L. Salomon, G. Chabrier and J.P. Goudonnet, Recent experimental results with the pstm: observation of a step on a quartz surface — spatial spectroscopy of microwaveguides, in D.W. Pohl and D. Courjon (eds.), *Near Field Optics*, NATO ASI Series E: Appl. Sci., Vol. 242, Kluwer, Dordrecht, 1993, p. 59.
- [29] B. Curtis, Paul Scherrer Institute, Zurich, Private communication, 1994.
- [30] D. Van Labeke and D. Barchiesi, Scanning tunneling optical microscopy: a theoretical macroscopic approach, *J. Opt. Soc. Am. A*, **9** (1992) 732.
- [31] N. Garcia, A direct solution to the inverse scattering problem in near-field optical microscopy: object structure reconstruction, *Opt. Lett.*, **20** (1995) 949.
- [32] E.J. Heller, M.F. Crommie, C.P. Lutz and D.M. Eigler, Scattering and absorption of surface electron waves in quantum corrals, *Nature*, **369** (1994) 4646.